Subduction megathrust heterogeneity characterized from 3-D seismic data

James D. Kirkpatrick[1], Joel H. Edwards[2], Alessandro Verdecchia[3], Jared W. Kluesner[4], Rebecca M. Harrington[3], Eli A. Silver[2]

[1]*Department of Earth and Planetary Sciences, McGill University, Montreal, Canada.*

[2]*Earth and Planetary Sciences, University of California Santa Cruz, Santa Cruz, CA, U.S.A.*

[3]*Ruhr University Bochum, Institute of Geology, Mineralogy and Geophysics, Bochum, Germany.*

[4]*Pacific Coastal and Marine Science Center, US Geological Survey, Santa Cruz, U.S.A.*

Megathrust roughness and structural complexity are thought to be significant controls on earthquake slip at subduction zones because they result in heterogeneity in shear strength and resolved stress. However, because active megathrust faults are difficult to observe, the causes and scales of complexity are largely unknown. Here, we measure the in-situ properties of the megathrust of the Middle America subduction zone in a 3-D seismic reflection volume to determine how fault properties vary. We quantify spatial variability in the megathrust roughness, overburden, and rock physical properties. Heterogeneity in the megathrust roughness exists at few-km length scales because the megathrust was dissected by active lower plate normal faults, which offset the megathrust and renewed fault roughness. Spatial variations in the rock physical properties at the plate interface are characterized by correlation length scales of hundreds of meters. Frontal prism taper, historical seismicity, and the variation in earthquake stress drop values local to the megathrust are all affected by the heterogeneity at these length scales. Both geometric and rheological complexities therefore control the mechanical behavior of the subduction plate interface, including earthquake rupture characteristics.

Seismological and geodetic observations suggest that the slip on a fault driven by plate motions is spatially and temporally complex [1,2]. When portions of faults rupture in earthquakes, rupture velocity, and slip durations and magnitudes within rupture areas vary spatially. Complexity is typically explained in terms of asperities on a fault, defined generally as high strength regions with elevated resolved stress[3]. Asperities are interpreted as frictionally strong or unstable areas that promote stick-slip type behavior and control the first order slip behavior of the fault[3]. High

stress areas on a fault may arise stochastically as earthquakes redistribute stress when they rupture parts of a fault, but asperity development may also be due to spatial variations in the roughness of a fault and/or the physical properties of the rocks in the fault zone[4]. Fault roughness is parameterized as the magnitudes of the local gradients on a non-planar surface, or, equivalently, the heights of bumps or topographic highs. Roughness contributes to fault strength[5], rupture complexity[6], and the extent of propagation[7,8], whereas the broad-scale geometry of a fault determines the tendency to creep or slip in great earthquakes[9]. Heterogeneity in properties such as friction, porosity, elastic moduli, and permeability should result in spatially variable effective stress field and slip behavior over the area of a megathrust[10,11].

Complexity is inherent to faults, but few data are available to determine the scales and magnitudes of variability in fault properties, the geologic controls on complexity, and how the resulting asperity population impacts earthquake rupture characteristics. In particular, measurements of fault properties over areas comparable to moderate to large earthquake ruptures (e.g. tens of kilometers) are extremely rare, so relating earthquake behavior to a specific fault attribute remains challenging. Instead, for subduction zones, the topography of the seafloor adjacent to a trench is often used as a proxy for megathrust roughness[10]. In this study, we use 3-D seismic reflection data located offshore Central America to measure for the first time the *in situ* characteristics of a subduction megathrust that extends from the trench to seismogenic depths. The results describe the fault at the scales necessary to evaluate which aspects of the underlying fault structure determine the distribution and scales of asperities.

Characteristics of the Central America Megathrust

The 3-D attributes of the Central America subduction plate boundary megathrust were defined from a pre-stack depth-migrated seismic reflection volume collected in 2011 near the Osa Peninsula[12-14] (Fig. 1). The volume is ~11 km-wide along-strike and extends to ~55 km landward of the trench. Here, we focus on the megathrust in the 30 km nearest to the trench, which images the fault to a maximum depth of around 6 km. Both vertical and horizontal resolution decrease with depth in the volume (see Methods).

The megathrust forms a shallow-dipping, continuous seismic reflection defined by substantial changes in seismic impedance across the fault zone (Fig. 1, 2). Structurally, the megathrust reflection separates underthrusted sedimentary and volcanic rocks from an intensely deformed margin wedge[13]. The peak wavenumber of the megathrust reflection suggests that the fault zone is relatively thin at shallow depths (~5 m), and becomes progressively thicker with depth (up to >100 m), consistent with drilling results offshore Nicoya[15] and exhumed systems[16].

The megathrust has substantial relief, with maximum roughness of up to ± ~500 m over the imaged region. Combined with the seafloor topography of the overlying wedge, these deviations cause the height of the lithostatic column above the fault to increase irregularly with distance from the trench (see contours in Fig. 1A). As a proxy for the normal stress resolved on the fault (average dip across the volume ~7°), this change in height suggests km-scale variability in resolved stress at a given depth.

At shallow depths, portions of the reflection appear corrugated[13] (Fig. 1A, 2A). Prominent corrugation axes are a few kilometers long with wavelengths of ~100-700 m and amplitudes of tens of meters. Corrugation axes trend 8-11° clockwise from the oblique convergence direction across the margin, close to the direction of the dip-slip component of the relative plate motions[13]. Along strike, at the same depth, corrugations are absent or only weakly developed[13]. Corrugations cannot be resolved deeper in the volume due to the reduced spatial resolution of the data with depth. However, we expect these features to be translated to greater depth by motion on the fault.

Normal faults that formed in response to bending of the subducted oceanic plate disrupt the megathrust at various depths in the volume (Fig. 2). These normal faults are spaced every few kilometers in the megathrust dip direction and trend at an acute angle to the megathrust strike, parallel to plate-bending normal faults observed to offset the seafloor to the west of the volume (Fig. 1B). In multiple places normal faults cut the megathrust, which re-formed at a different structural level in response[13]. Abandoned segments of the megathrust that truncate against a normal fault can be identified above or below the re-formed and immature active megathrust (Fig. 2)[17]. The along-strike structure of the plate-bending normal faults includes bends and

stepovers and the interaction between the normal faults and megathrust is geometrically complex in places. For example, at around 5-7 km landward of the trench, the dip of the megathrust increases across a pair of overlapping normal faults (Fig 1A). The megathrust has re-formed adjacent to the more southeasterly fault but not the northwesterly. Consequently, the more recently formed megathrust extends further up-dip on the southeast side of the volume. Approximately linear topographic highs in the region ~9-30 km from the trench correspond closely to horsts in the subducted plate formed by plate-bending faults, which indicate the normal faults distort the megathrust geometry at all observed depths.

The roughness of the megathrust reflection increases as a power law function of the length scale of observation (Fig. 3). The scaling exponent to a power law fit through the calculated power spectral density roughness as a function of wavelength, known as the Hurst exponent, H, is < 1 averaged over the horizon (see Methods). Overall, the roughness is consistent with m-scale observations of exhumed ancient faults[18] (Extended Data Fig. 1). At length scales less than a few kilometers, the reflection is, on average, weakly anisotropic, with smoother profiles in the down-dip direction (Fig. 3B). However, the dip- and strike-directions are indistinguishable at length scales greater than a few km (Fig. 3B, see also Extended Data Fig. 2) because H is greater in the dip direction (~0.7) than in the strike direction (~0.6). The length scale at which this isotropic geometry is attained is approximately the spacing between plate-bending normal faults at the edges of the ridges in the megathrust.

Heterogeneity in megathrust properties

Within the power-law scaling, heterogeneity in the roughness exists when areas of the fault with dimensions corresponding to the normal fault spacing are compared (Fig. 3B). This heterogeneity is most evident in the best-resolved portion of the data where the corrugated and weakly-corrugated sub-areas of the shallow megathrust are juxtaposed along strike. In both regions the megathrust is smoother parallel to the corrugations compared to perpendicular to the corrugations, consistent with the overall average behavior. However, the non-corrugated regions are rougher than the corrugated regions in both directions. As shown in Fig. 2A, the rough, weakly-corrugated geometry corresponds to the region where the megathrust recently reformed because it was offset by the southeasterly of the two overlapping normal faults described above.

The more corrugated areas, which have not been offset, are more mature and represent a relative reduction in roughness, and a concomitant change in the surface geometry toward an anisotropic topography, suggesting they formed by wear during slip[19]. The roughness of a relict patch of the megathrust is intermediate between the corrugated and non-corrugated patches (Extended Data Fig. 3), implying that offset by normal faulting rather than slip-related megathrust roughness is the primary factor in determining when and where the megathrust is disrupted and abandoned.

Compared to the adjacent seafloor, the megathrust is rough at length scales less than ~2 km (Fig. 3B). Only the smoothest part of the fault, the corrugated patch aligned with slip, has similar roughness to the seafloor. These observations indicate the megathrust geometry approximates the seafloor at broad scales, but modification of the megathrust by deformation during slip and offsets across plate-bending normal faults roughen the megathrust compared to the seafloor.

The amplitude of the active megathrust fault reflection varies from regions of strongly to weakly reversed polarity relative to the seafloor reflection, implying the physical properties of the rocks that control seismic impedance at the plate interface are variable[12,20] (Fig. 3). Geostatistical analysis (see Methods) of the reflection amplitude variations shows they are described by a characteristic distance of ~300-600 m, beyond which separated values are no longer spatially correlated (defined by the separation distance, h, at which the data in Fig. 3D attain a constant value). The non-corrugated portions of the fault at shallow depth do not exhibit a correlation distance, so are nonstationary along the corrugation direction. Additionally, periodicity in the amplitudes within the corrugated areas shows the spatial distribution of amplitudes correlates with the development of the corrugation structures (Fig. 3D).

Implications for fault mechanics

Spatial variations in fault roughness, lithostatic load, and physical properties (pore pressure and/or elastic moduli) imply effective stress variability on the Costa Rica subduction plate interface. This spatial variability therefore defines asperities, which according to our results are defined by both geometry and physical properties.

Where offsets across plate-bending normal faults forced the megathrust to propagate to a new position, the megathrust is rougher (Fig. 3B), and therefore stronger[5], than more well-established smoother areas. The areas of rough megathrust between normal faults correspond directly to seismic asperities and have dimensions of around a few kilometers. Offsets across normal faults also roughen the megathrust at scales larger than the spacing between them by imposing relief onto the megathrust. This relief causes the measured roughness to be isotropic at length scales greater than the normal fault spacing. Normal-sense earthquakes commonly occur in the subducting slab beneath seismogenic subduction megathrusts [21,22], suggesting the processes documented here that affect megathrust roughness may be common to subduction margins. Due to the consistent spacing of the plate-bending faults, the dimensions of areas with different roughness are approximately similar within the volume. This similarity indicates a causative link between the thermal structure of the oceanic plate, which determines the elastic thickness and spacing of plate-bending normal faults, and seismicity patterns on the subduction interface.

Juxtaposition of different lithologies with different competence and porosity or permeability can explain the spatial variation in mechanical properties inferred from the variable megathrust reflection amplitude. Heterogeneity in rock physical properties is the inevitable consequence of offsets observed across plate-bending normal faults and also imbrication within the plate boundary zone. Similar juxtaposition of accretionary wedge rocks against subducted sedimentary rocks and potentially basaltic crust is evident in map-scale distributions of lithologies within ancient subduction complexes[23].

Geomorphological and seismological characteristics of the subduction zone suggest that the asperities defined by our results control the mechanical behavior of the megathrust. The taper angle of the frontal prism is lower (~10.5-11.5°) where the megathrust is smooth and well-corrugated, compared to where it is rougher (~12-14°) (Fig. 1C), indicating megathrust roughness contributes to long-term fault strength[24]. Historical records suggest the largest magnitude earthquake on this portion of the margin is approximately M7[25]. Earthquake rupture propagation is restricted on rough faults because of the local variability in the resolved shear stress[8]. Roughening of the megathrust by plate-bending normal fault offsets may restrict rupture area, particularly limiting rupture propagation up-dip. The particularly shallow hypocentral depth

of the 2002 Mw 6.4 Osa earthquake[26] may also have resulted from the relatively rough megathrust.

Source parameters of earthquakes local to the megathrust also show the effect of the observed megathrust geometry on earthquake slip (Fig. 4; see Methods for details). Stress drops vary widely for earthquakes with small dimension (less than a few hundred m in Fig. 4). Earthquakes with larger dimensions have a narrower range of stress drops for a given rupture dimension (Fig. 4), indicating they are less sensitive to megathrust variability because they propagate through, and average-out the heterogeneity. Due to an uneven number of recordings at different corner frequencies, the stress drop populations shown in Fig. 4 should not be interpreted as a true measure of a dimension across which event populations are different. Differences in stress drop variability at small and large scales are consistent with the fractal geometry of the fault[27]. However, these two populations are separated by a dimension that corresponds closely to the characteristic length scales in the seismic reflection amplitude suggesting the stress drops are sensitive to the causes of variability in seismic impedance, likely pore pressure. Although the majority of the epicentral locations of the analyzed events are located down dip of the reflection volume, the asperities defined by both geometry and physical property variability described above must translate down dip over geologic time and so be present deeper in the system as well. We therefore postulate that the observed stress drops are primarily the result of rheological asperities within the megathrust system.

These results provide new insight into the mechanics of earthquakes by defining how geological processes at the subduction interface lead to the development of a population of asperities, and thus stress conditions, that control seismic slip. The relatively small dimension of the asperities suggests that small scale variability in slip behavior of earthquakes may result from heterogeneity in fault properties, whereas variability between larger events may be due to rupture dynamics[1]. The causes and scales of structural complexity should be explored as a control on global variations in earthquake source parameters[28].

References

1 Ye, L. L., Kanamori, H. & Lay, T. Global variations of large megathrust earthquake rupture characteristics. *Science Advances* **4**, doi:10.1126/sciadv.aao4915 (2018).
2 Loveless, J. P. & Meade, B. J. Two decades of spatiotemporal variations in subduction zone coupling offshore Japan. *Earth and Planetary Science Letters* **436**, 19-30, doi:10.1016/j.epsl.2015.12.033 (2016).
3 Lay, T., Kanamori, H. & Ruff, L. THE ASPERITY MODEL AND THE NATURE OF LARGE SUBDUCTION ZONE EARTHQUAKES. *Earthquake Prediction Research* **1**, 3-71 (1982).
4 Noda, H. & Lapusta, N. Three-dimensional earthquake sequence simulations with evolving temperature and pore pressure due to shear heating: Effect of heterogeneous hydraulic diffusivity. *J. Geophys. Res.-Solid Earth* **115**, doi:10.1029/2010jb007780 (2010).
5 Fang, Z. J. & Dunham, E. M. Additional shear resistance from fault roughness and stress levels on geometrically complex faults. *J. Geophys. Res.-Solid Earth* **118**, 3642-3654, doi:10.1002/jgrb.50262 (2013).
6 Shi, Z. Q. & Day, S. M. Rupture dynamics and ground motion from 3-D rough-fault simulations. *J. Geophys. Res.-Solid Earth* **118**, 1122-1141, doi:10.1002/jgrb.50094 (2013).
7 Yu, H. Y., Liu, Y. J., Yang, H. F. & Ning, J. Y. Modeling earthquake sequences along the Manila subduction zone: Effects of three-dimensional fault geometry. *Tectonophysics* **733**, 73-84, doi:10.1016/j.tecto.2018.01.025 (2018).
8 Bletery, Q. *et al.* Mega-earthquakes rupture flat megathrusts. *Science* **354**, 1027-1031, doi:10.1126/science.aag0482 (2016).
9 Gao, X. & Wang, K. L. Strength of stick-slip and creeping subduction megathrusts from heat flow observations. *Science* **345**, 1038-1041, doi:10.1126/science.1255487 (2014).
10 Wang, K. L. & Bilek, S. L. Invited review paper: Fault creep caused by subduction of rough seafloor relief. *Tectonophysics* **610**, 1-24, doi:10.1016/j.tecto.2013.11.024 (2014).
11 Ikari, M. J., Niemeijer, A. R., Spiers, C. J., Kopf, A. J. & Saffer, D. M. Experimental evidence linking slip instability with seafloor lithology and topography at the Costa Rica convergent margin. *Geology* **41**, 891-894, doi:10.1130/g33956.1 (2013).
12 Bangs, N. L., McIntosh, K. D., Silver, E. A., Kluesner, J. W. & Ranero, C. R. Fluid accumulation along the Costa Rica subduction thrust and development of the seismogenic zone. *J. Geophys. Res.-Solid Earth* **120**, 67-86, doi:10.1002/2014jb011265 (2015).
13 Edwards, J. H. *et al.* Corrugated megathrust revealed offshore from Costa Rica. *Nature Geoscience* **11**, 197-+, doi:10.1038/s41561-018-0061-4 (2018).
14 Kluesner, J. W. *et al.* High density of structurally controlled, shallow to deep water fluid seep indicators imaged offshore Costa Rica. *Geochemistry Geophysics Geosystems* **14**, 519-539, doi:10.1002/ggge.20058 (2013).
15 Tobin, H., Vannucchi, P. & Meschede, M. Structure, inferred mechanical properties, and implications for fluid transport in the decollement zone, Costa Rica convergent margin. *Geology* **29**, 907-910, doi:10.1130/0091-7613(2001)029<0907:simpai>2.0.co;2 (2001).
16 Rowe, C. D., Moore, J. C., Remitti, F. & Scientist, I. E. T. The thickness of subduction plate boundary faults from the seafloor into the seismogenic zone. *Geology* **41**, 991-994, doi:10.1130/g34556.1 (2013).

17 Bangs, N. L., McIntosh, K. D., Silver, E. A., Kluesner, J. W. & Ranero, C. R. A recent phase of accretion along the southern Costa Rican subduction zone. *Earth and Planetary Science Letters* **443**, 204-215, doi:10.1016/j.epsl.2016.03.008 (2016).
18 Brodsky, E. E., Kirkpatrick, J. D. & Candela, T. Constraints from fault roughness on the scale-dependent strength of rocks. *Geology* **44**, 19-22, doi:10.1130/g37206.1 (2016).
19 Dascher-Cousineau, K., Kirkpatrick, J. D. & Cooke, M. L. Smoothing of Fault Slip Surfaces by Scale-Invariant Wear. *J. Geophys. Res.-Solid Earth* **123**, 7913-7930, doi:10.1029/2018jb015638 (2018).
20 Bangs, N. L. B. *et al.* Broad, weak regions of the Nankai Megathrust and implications for shallow coseismic slip. *Earth and Planetary Science Letters* **284**, 44-49, doi:10.1016/j.epsl.2009.04.026 (2009).
21 Choy, G. L. & Kirby, S. H. Apparent stress, fault maturity and seismic hazard for normal-fault earthquakes at subduction zones. *Geophysical Journal International* **159**, 991-1012, doi:10.1111/j.1365-246X.2004.02449.x (2004).
22 Okuwaki, R. & Yagi, Y. Rupture Process During the M-w 8.1 2017 Chiapas Mexico Earthquake: Shallow Intraplate Normal Faulting by Slab Bending. *Geophys. Res. Lett.* **44**, 11816-11823, doi:10.1002/2017gl075956 (2017).
23 Regalla, C., Rowe, C., Harrichhausen, N., Tarling, M. & Singh, J. in *Geology and Tectonics of Subduction Zones: A Tribute to Gaku Kimura GSA Special Paper* (eds T. Byrne *et al.*) 155-174 (2018).
24 Dahlen, F. A. CRITICAL TAPER MODEL OF FOLD-AND-THRUST BELTS AND ACCRETIONARY WEDGES. *Annual Review of Earth and Planetary Sciences* **18**, 55-99, doi:10.1146/annurev.ea.18.050190.000415 (1990).
25 DeShon, H. R. *et al.* Seismogenic zone structure of the southern Middle America Trench, Costa Rica. *J. Geophys. Res.-Solid Earth* **108**, doi:10.1029/2002jb002294 (2003).
26 Arroyo, I. G., Grevemeyer, I., Ranero, C. R. & von Huene, R. Interplate seismicity at the CRISP drilling site: The 2002 Mw 6.4 Osa Earthquake at the southeastern end of the Middle America Trench. *Geochemistry Geophysics Geosystems* **15**, 3035-3050, doi:10.1002/2014gc005359 (2014).
27 Candela, T., Renard, F., Bouchon, M., Schmittbuhl, J. & Brodsky, E. E. Stress Drop during Earthquakes: Effect of Fault Roughness Scaling. *Bulletin of the Seismological Society of America* **101**, 2369-2387, doi:10.1785/0120100298 (2011).
28 Denolle, M. A. & Shearer, P. M. New perspectives on self-similarity for shallow thrust earthquakes. *J. Geophys. Res.-Solid Earth* **121**, 6533-6565, doi:10.1002/2016jb013105 (2016).

Correspondence and requests for materials should be addressed to James Kirkpatrick

james.kirkpatrick@mcgill.ca

Acknowledgements

Thanks to Nathan Bangs, Kirk McIntosh, and the crew of the R/V Langseth for their efforts acquiring and processing the data. Thanks also to Matt Ikari and an anonymous reviewer for constructive comments that substantially improved the manuscript and to Jamie Conrad for feedback on an early version of the manuscript. This work was supported by the Natural Sciences and Engineering Research Council of Canada (NSERC), Discovery Grant RGPIN-2016-04677 (JK) and the National Science Foundation (NSF) grants OCE-0851529 and OCE-0851380.

Author contributions

The study concept was formulated by JDK, JWK and RMH. JHE applied post processing, performed amplitude-driven tracking, and extracted geometric attributes of the megathrust. Geometric data validation and analysis was carried out by JHE, JDK, JWK, and EAS. AV and RH completed source parameter analyses. JDK wrote the manuscript with contributions from all other authors.

Financial and non-financial competing interests

Authors declare no competing interests.

Figures

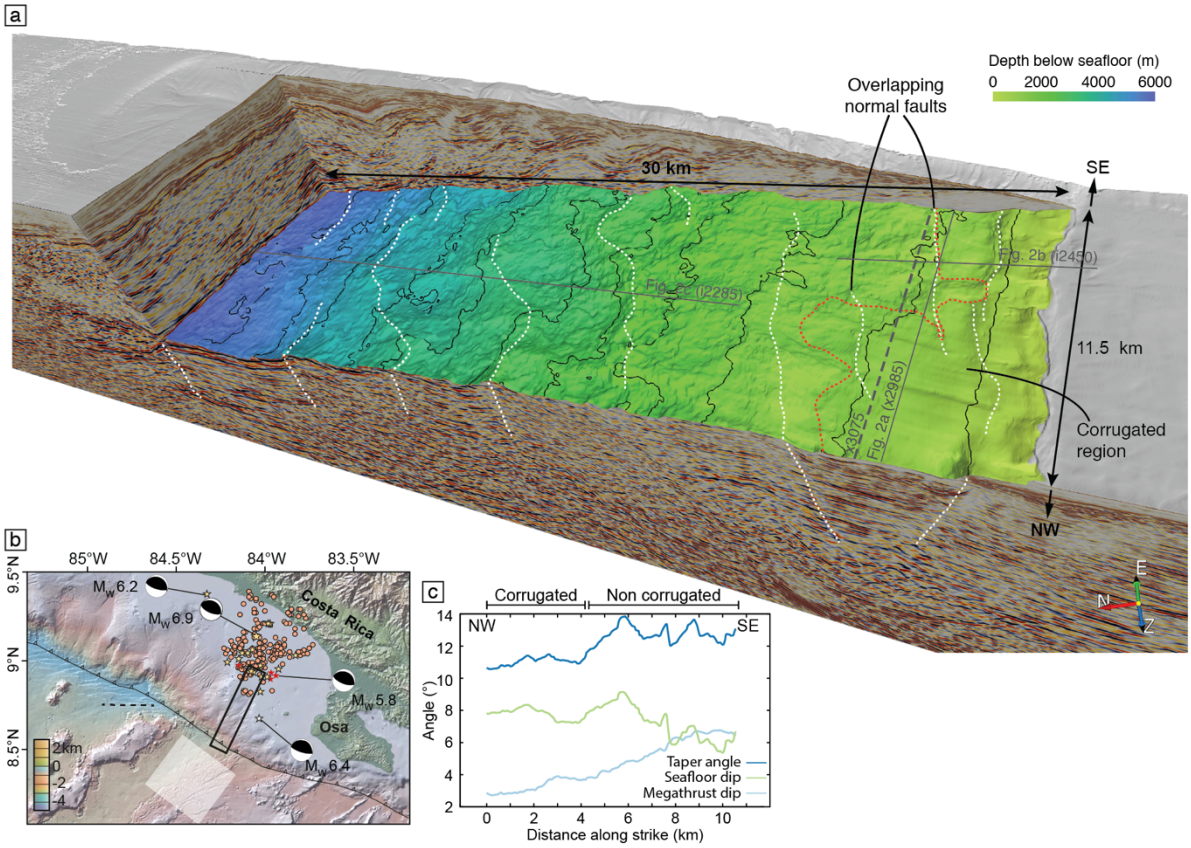

Figure 1. Characteristics of the megathrust. A. Perspective view of the megathrust with the upper plate cut away. Black lines are contours showing meters below sea floor (500 m intervals). Dashed white lines are megathrust - plate-bending normal fault (throw greater than ~100 m) intersections. Red dashed line indicates the extent of re-formed megathrust in the shallow part of the volume. The megathrust is relatively immature, down-dip of the line. B. Map showing the location of the seismic volume and earthquake epicenters of events shown in Fig. 4. White square shows the region from which seafloor roughness was calculated; dashed line shows trend of plate-bending normal faults cutting the seafloor. C. Wedge taper, seafloor slope and dip of megathrust calculated for each crossline in the inline direction averaged from the trench (x2675) to ~5 km from the trench (x3075 – shown in part a).

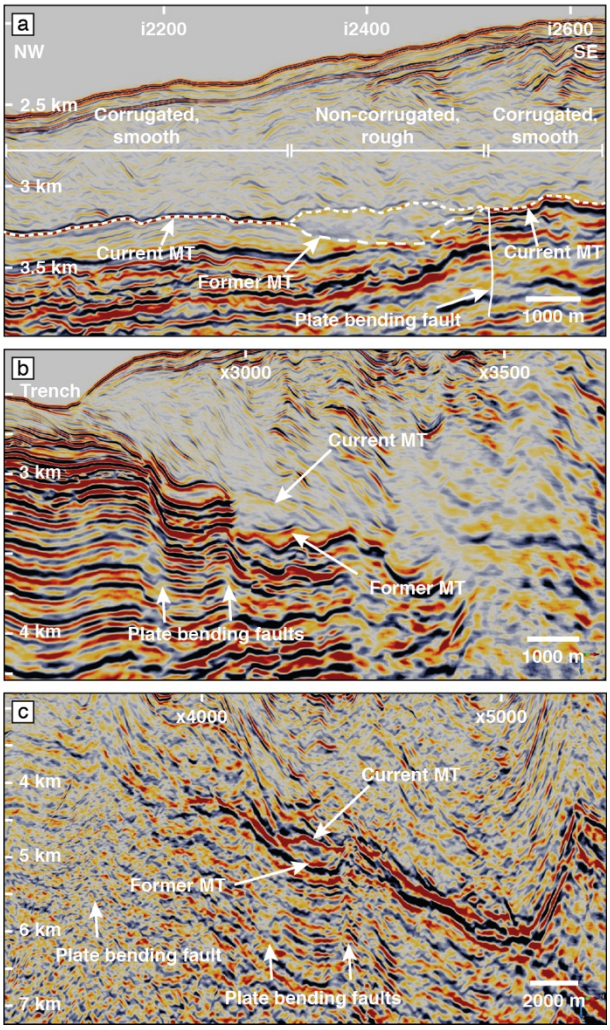

Figure 2. Dissection of the megathrust by plate-bending normal faults. A. Crossline (trench parallel) section showing corrugated and non-corrugated regions of the megathrust (MT) separated by a plate bending normal fault (section location shown in Fig. 1A). B. Inline (trench perpendicular) section showing an example of the megathrust offset by normal fault at shallow depth. C. Inline showing a former MT horizon truncated against a plate-bending normal fault from deeper in the volume. For all sections, numbers at the top show reference inlines or crosslines through the volume, numbers one the left side show the depth below seafloor, and the horizontal scale is shown in the lower left.

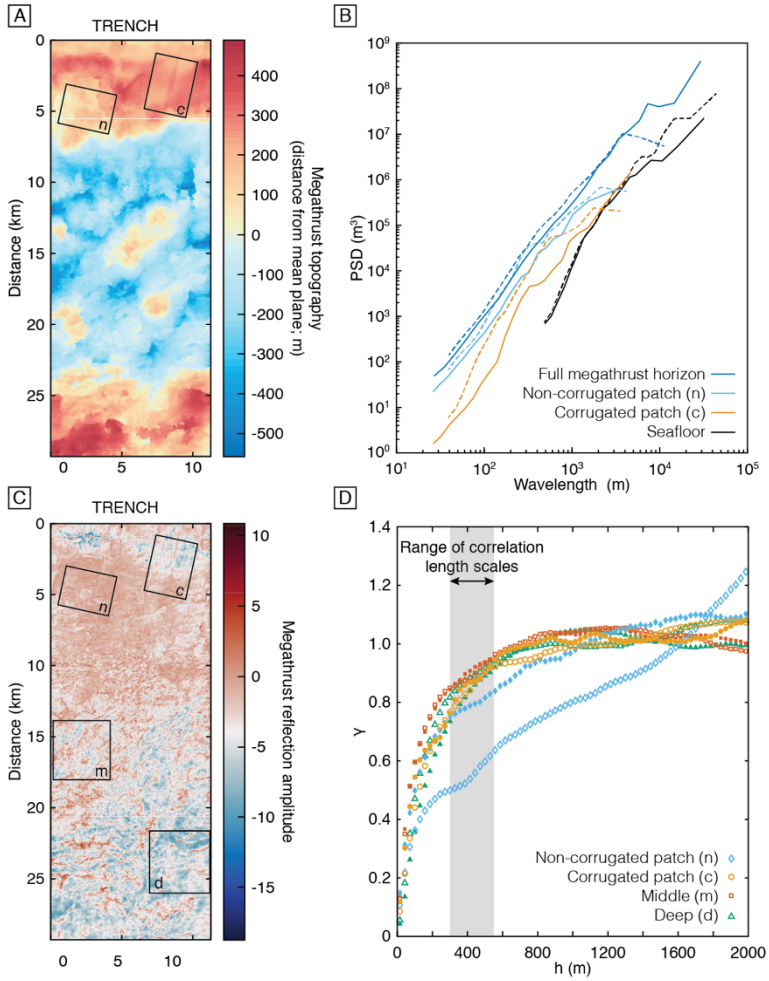

Figure 3. Analysis of the megathrust reflection. A. Fault topography. B. Power spectral density roughness calculated for the full megathrust, two sub-regions of the megathrust shown in A, and the seafloor adjacent to the trench. Solid lines are the dip direction for the overall fault dataset, the corrugation direction for n and c, and plate-bending normal fault strike direction for the seafloor region. Dashed lines are perpendicular to these reference directions in each case. C. Amplitude of the fault reflection. D. Experimental variogram normalized by dataset variance calculated for regions of the fault reflection amplitude field shown in C. Hollow symbols are down dip (middle, deep regions), or along corrugation axes (n, c). Filled symbols are perpendicular to these reference directions.

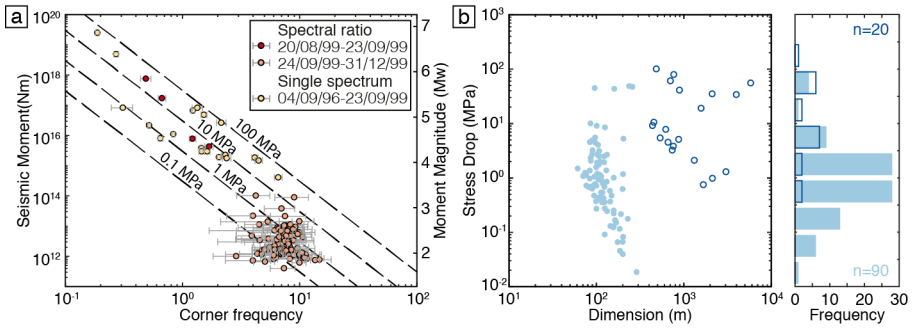

Figure 4. Analysis of earthquake source parameters. A. Station-averaged corner frequency versus station-averaged seismic moment calculated for the earthquakes from the three catalogs. Events with corner frequencies greater than ~25 Hz were not analyzed due to signal:noise limitations. Error bars indicate 95% confidence intervals of each corner frequency estimate. B. Stress drop as a function of station-averaged source dimension for all earthquakes. Solid symbols correspond to events with corner frequency (fc) > 2.5 Hz, hollow symbols are events with fc < 2.5 Hz. Histogram to right shows distribution of $\Delta\sigma$ in each group.

Methods

Seismic Reflection Volume

We utilized the 3-D pre-stack Kirchoff migrated depth seismic reflection volume[29] collected by the R/V *Marcus G. Langseth* and processed by CGG Veritas and Repsol between 2011 – 2013 [12]. The volume consists of ~12.5 x 18.75 m binned depth-converted seismograms with geologic imagery up to 10 km subseafloor across the outer shelf, slope and trench offshore the Osa Peninsula over an ~11 x 55 km^2 area. The volume has a "thin-bed" vertical resolution[30] that decreases with depth from ~5 m to ~125 m (assuming ¼ dominant wavelength resolvability[31]). Horizontal resolution decreases from the nominal ~12.5 x 18.75 m binning to ~100-300 m for the deepest parts of the megathrust (Extended Data Fig. 4).

The megathrust is generally defined as the reflection that separates landward-dipping reflections of the accretionary wedge from sub-parallel reflections corresponding to subducted seafloor sedimentary rocks [13]. However, when the megathrust changed its structural position adjacent to steeply dipping plate-bending faults, it moved upsection into the overlying accretionary wedge, cutting across landward-dipping reflections. At the locations where this happened, a relict megathrust is observed downsection from its original position, separating underthrusted, undeformed sediments from the accretionary wedge.

Even with high fold and a highly tuned broadband seismic source, the resulting 3-D seismic imagery does not overcome the loss of high frequencies with outward wave propagation and increasing depth (Extended Data Fig. 4), resulting in increasing breadth of the recorded wavelet [31]. Because we focused on the geometry of the megathrust in 3-D (i.e., the top surface of the subducting plate), the horizontal and vertical resolution (i.e., megathrust positional changes in space that are detected by seismic imagery) is inversely proportional to the bandwidth of the frequency spectrum (i.e., tightness of the source pulse [30]). With increasing depth, frequency bandwidth progressively loses the higher frequency components (Extended Data Fig. 4), resulting in decreasing megathrust resolvability. In the depth volume, this results in an increasing post-migration Fresnel zone (dominant wavenumber / 4; [32]) with increasing depth (Extended

Data Fig. 4), with Fresnel zone values ranging from ~5 meters near the trench to >90 meters at >5 km subseafloor.

We performed post-stack processing to remove random noise and augment amplitude driven tracking. This processing included calculating iterative apparent dip (inline and crossline direction) volumetric calculations and performing subsequent median filtering with varying stepouts (inline and crossline direction) guided by preceding apparent dip calculations. By doing this process iteratively (i.e., by incrementally increasing stepout sizes (1x1, 2x2, etc.)), we empirically resolved the effects of stepout size on megathrust roughness (e.g., Extended Data Fig. 2). The significance of this smoothing changed with depth, effecting the shallow portion of the megathrust at scales ≤ 100 m, and the deeper portions at scales smaller than around a few hundred meters. The smoothing generally removes random noise or features below the resolution of the data without changing the geometry of features that are visually well-resolved. However, we use these values as limits on the highest-resolution geometry in the following analyses.

Megathrust mapping efforts were performed within OpendTect v6.2.5. Mapping was done on dip-steered (i.e., apparent dip and dip direction guided) median filtered data and used an iterative workflow of interpreter picks and amplitude-driven auto tracking (helping us avoid inline / crossline horizon biases) constrained by a look window and acceptable amplitude threshold (% amplitude deviation from interpreter seed pick). The workflow is generally as follows: 1) load a designated subset of the reflection volume, 2) start / load megathrust horizon, 3) pick several seismogram megathrust locations, called seeds, 4) input allowed amplitude thresholds and look window (in depth), 5) 3-D auto-track outward from seed picks using the apparent dip volume to guide the look window, 6) QC results and delete errant portions of the horizon, 7) if results are egregiously errant or are too conservative, either change the look window or acceptable amplitude threshold, and 8) lock remaining seeds and repeat.

Roughness Measurements

We measured the roughness of the megathrust horizon by calculating the power spectral density (PSD) as a function of wavenumber from cross sections through the seismic reflection

corresponding to the megathrust [18]. The megathrust was extracted from the reflection volume as a series of regularly-spaced points with 3-dimensional coordinates. The points on the fault surface were transformed from 3-dimensional to 2-dimensional $Z(X,Y)$) by rotating the data so that Z was perpendicular to the mean plane through the entire dataset (Fig. 3A). PSD was calculated from discretized sections through the rotated data oriented in the inline and crossline directions and parallel and perpendicular to local corrugation axes, where present, as representative of the slip-parallel and slip-perpendicular directions. For each profile the height of the surface, $z(x)$, was found and any linear trend removed. The PSD, the square of the modulus of the Fourier transform of the profile, was calculated as a function of wavenumber from a FFT of $z(x)$. A cosine taper applied over 3% of the data minimized leakage. Results were averaged for thousands of strike-parallel and hundreds of dip-parallel profiles, and the resulting spectra converted to spatial length scale for use as a measure of the how much the fault deviates from a planar surface as a function of observation length scale. For each dataset and subset analyzed, $\mathrm{PSD}(\lambda) = C\lambda^{(2H+1)}$, where PSD is the average power spectral density (a measure of the deflection of the reflection from a planar surface) calculated at a length scale, λ, C is a constant, and H is the Hurst exponent.

Waveform Analysis

Here we use waveform data from September 1999 to November 1999 recorded by 5 short-period land stations (40 Hz sampling rate) and 12 broadband ocean bottom (OBS) stations (64 Hz and 128 Hz sampling rates) from the CRSEIZE experiment (Extended Data Table 1). The continuous data recorded part of the aftershock sequence following the M_w 6.9, 20 August 1999, Quepos earthquake that occurred on the plate boundary thrust fault along southern Costa Rica.

Waveforms were sourced from three catalogs (Extended Data Fig. 5, Extended Data Table 1): 1. aftershocks from the M 6.9 mainshock (20/08/1999) recorded by the ocean bottom seismometer broadband stations (CRSEIZE) relocated by [25]; 2. aftershocks that occurred before the deployment of the CRSEIZE network recorded by land stations of the Costa Rican (SJS) and IRIS (JTS) networks; 3. earthquakes recorded by SJS and JTS networks that occurred between

04/09/1996 and 23/09/1999, including a M 6.9 mainshock (20/08/1999) were also included to extend the observed magnitude range.

Starting with a list of 259 relocated aftershocks (M 0.4 to M 3.6) taken from [25], we select the 188 events with hypocenter relocations within 10 km of the plate boundary interface. In order to estimate seismic moments of the individual events, we cut the waveform data into 2 s window beginning 0.5 s before the respective P- and S-wave arrivals, and calculate the spectral amplitude using Thomson's multi-taper method [33] by fitting the spectrum with the Brune spectral model [34,35]:

$$\Omega(f) = \frac{\Omega_0 e^{\frac{-\pi f t}{Q}}}{\left[1+\left(\frac{f}{f_c}\right)^{\gamma n}\right]^{\frac{1}{\gamma}}}, \quad (1)$$

where Ω_0 is the long-period spectral amplitude, f is the spectral frequency, f_c is the corner frequency, n is the high-frequency fall-off rate, γ is a constant commonly set to 2 [36], Q is the quality factor (set equal to 1000), and t is the travel time, calculated using the hypocenter relocation and the velocity model from [25]. We then calculate the moment using the fitted Ω_0 values in the following:

$$M_0 = \frac{4\pi c^3 R \Omega_0}{U_{\phi\theta}}, \quad (2)$$

where ρ (kg/m^3) is the density, c (m/s) is the P- or S-wave speed at the depth of the hypocenter taken from the velocity model of [25], R is the distance from the event determined using the hypocenter relocation from [25], and $U_{\phi\theta}$ is the mean radiation pattern of 0.52 for P waves and 0.63 for S waves [37].

Robust estimations of corner frequency require site and path effects (i.e., all non-source related effects) to be removed from the waveform data. We used a spectral ratio approach, which uses the ratio of small, co-located earthquake pairs recorded on a given station to cancel all non-source related effects in frequency space, allowing for accurate estimations of the corner

frequency from one, or both, events in the pair, depending on the frequency range of high signal-to-noise ratio [38].

Two earthquakes that are co-located, thus rupture the same patch of a fault, should have similar waveforms (Extended Data Fig. 6). To find an event pair that is co-located (with an even more conservative estimation of co-location than given by hypocentral errors) we first select co-located events pairs with cross-correlation coefficient larger than 0.7 [39], and magnitude difference larger than 0.5. The latter requirement helps to identify event pairs with corner frequency values that differ enough to be resolved in the spectral ratio fitting. We then model the spectral ratios at frequencies where the signal-to-noise ratio (SNR) for both earthquakes is above 3 over the frequency band, obtaining corner frequency estimates by fitting each individual spectral ratio using the analytical expression for the ratio of two spectra:

$$\Omega_r(f) = \Omega_{0r}\left[\frac{1+\left(\frac{f}{f_{c2}}\right)^{\gamma n}}{1+\left(\frac{f}{f_{c1}}\right)^{\gamma n}}\right]^{\frac{1}{\gamma}}, \qquad (3)$$

where Ω_{0r} is the displacement amplitude spectral ratio, f is the frequency, f_{c1} and f_{c2} are the corner frequencies of the large and small earthquakes, n is the high-frequency fall-off (assumed equal to 2), and γ is a constant that controls the shape of the curvature around the corner frequency (Extended Data Fig. 6). The values of n and γ are typically characteristic of a data set within a given region. We test both the Brune [34] model ($\gamma = 1$) and Boatwright [36] model ($\gamma = 2$), and use the sharper-cornered model from [36] because it gives a better fit to the majority of the spectral ratios, as also shown [40] in New Zealand. Due to the SNR > 3 requirement we were not able to resolve events with f_c over ~25 Hz.

Once we have estimated an initial f_{c1} using a least-squares fit, we vary f_{c1} by 0.2 Hz before and around the original value, using the new corner frequencies as fixed parameters to estimate confidence intervals in which the corner frequency values provide a misfit within 5% of the original fit [41]. After calculating and plotting the normalized variance, we discard those couples with variance that do not form a parabola, and we take the f_{c1} with the minimum variance as final

value [41]. As the SNR > 3 requirement does not typically extend to frequencies of at least 10 Hz above the initial f_{c2} estimate in our data, we do not use the estimated f_{c2} value.

No sufficiently similar event pairs in the dataset recorded by SJS and JTS networks that occurred between 04/09/1996 and 23/09/1999 were recorded with a signal-to-noise ratio > 3 over a wide frequency band, so source parameters were calculated from a single spectrum. Seismic moments (M_0) calculated from single spectra, and corner frequencies (f_c) calculated from the spectral ratio analysis are used as input to obtain stress drop values ($\Delta\sigma$) adopting the circular model of Eshelby [42]:

$$\Delta\sigma = \frac{7}{16}\frac{M_0}{r^3}, \quad (4)$$

and the source radius (r) from Madariaga [43] model:

$$r = \frac{k\beta}{f_c}, \quad (5)$$

where β is the shear wave velocity at the hypocentral depth [25] and k is 0.315 for P-waves and 0.21 for S-waves. If one uses a different geometry (e.g., square rupture), the constant on the right side of equation (4) will change slightly, but is still on the order of unity, thus much smaller than the anticipated error in estimated stress drop.

Because the CRSEIZE stations deployment took place approximately one month (between September 16th and September 26th, 1999) after the start of the seismic Osa seismic sequence, the mainshock and moderate aftershocks of M >4.2 were not recorded by the array. In order to obtain corner frequency estimates of some of the larger-magnitude aftershocks, we use waveform data from Red Sismologica Nacional de Costa Rica (RSN(UCR-ICE)); station SJS, doi:10.15517/TC) and the IRIS/IDA Seismic Network (station JTS; doi:10.7914/SN.II) to calculate spectral ratios for four aftershocks that occurred a few days after the 20 August 1999, M_w 6.9 mainshock (Extended Data Table 1). Due to the larger magnitudes, and thus the anticipated longer source-time functions (as moment is expected to scale with the cube of the

duration), we cut the waveform data for these four events into 7 s windows beginning 0.5 s before the respective P- and S-wave arrivals. As for the smaller earthquakes, we calculate the seismic moment of these four events using Brune spectral fits (Equation 1) [34] to long-period amplitudes. Additionally, in order to investigate moment-corner frequency scaling over a broader range of magnitudes, we calculate source parameters for several M >3.5 earthquakes that occurred in the same region between September 1996 and September 1999. Because for these events we could not find co-located events pairs with cross-correlation coefficient larger than 0.7 with the available seismic station coverage, we calculate corner frequencies (f_c) from single spectra (Equation 1).

In total, stress drop was calculated for 110 events with moments ranging from 4.0×10^{11} to 2.5×10^{19} Nm. Earthquakes with corner frequencies, f_c, >2.5 Hz and source dimensions less than a few hundred m have stress drops, $\Delta\sigma$, that vary by over 3 orders of magnitude (0.019 to 49 MPa, mean = 3.5 MPa, n = 90). Events with f_c < 2.5 Hz and dimensions larger than a few hundred m have systematically higher $\Delta\sigma$ with a spread of around 2 orders of magnitude (0.75 to 100 MPa, mean = 24 MPa, n = 20). These populations are statistically different to a 1% significance level. The threshold corner frequency between these populations was chosen from visual inspection of the data shown in Fig. 4. Due to an uneven number of recordings at different magnitudes, this threshold is intended to illustrate the difference between large and small events rather than as a true measure of a dimension across which event populations are different.

Statistical Analysis of Megathrust Reflection Amplitudes

The waveform of the fault reflection is controlled by the impedance (the product of seismic velocity and density) contrast across the fault, and has been used to map impedance variations as a proxy for physical properties in previous 3-D seismic reflection data [12,20]. In our dataset, the fault reflection amplitude (extracted with automatic gain control) varies from regions of strongly to weakly reversed polarity (relative to the seafloor reflection) over distances of hundreds of meters (see Fig. 3C in the main text). Spatial continuity in the amplitude variation was analyzed by calculating the experimental variogram, $\gamma(h)$ [44], along reference directions for representative areas of the fault:

$$\gamma(h) = \frac{1}{2N(h)} \sum_{i=1}^{N} [d(x+h) - d(x)]^2, \qquad (6)$$

where $d(x)$ represents the fault reflection amplitude at a particular location x, $d(x+h)$ is the value of the amplitude at location $x+h$, where h is the separation distance, or lag (m), and $N(h)$ is the number of data pairs separated by h. A plot of calculated $\gamma(h)$ vs. h is referred to as an experimental variogram.

In a stationary field, $\gamma(h)$ attains a constant value that is approximately equal to the variance of $d(x)$ [44]. This constant value is known as the sill, which is represented by a plateau in the experimental variogram. The distance at which the sill is reached is the correlation distance, α, also called the range parameter. The range represents a characteristic distance beyond which separated values are, on average, no longer correlated. $\gamma(h)$ values less than the sill for $h < \alpha$ indicate spatial structure in a dataset. Fractal datasets, such as fault surfaces mapped from exposures of exhumed ancient faults, result in $\gamma(h)$ that increases continuously for all values of h. Reference directions along which the variogram was calculated correspond to the directions that the roughness was measured (i.e. down dip and across strike, or parallel to and perpendicular to corrugations, where evident). Calculations were performed in Matlab with the function Experimental (Semi-) Variogram [45], and checked with the Stanford Geostatistical Modeling Software (SGeMS) [46]. Four subregions of the reflection were chosen for analysis as representative of different portions of the fault: the corrugated and non-corrugated portions at shallow depth, one region from the middle of the volume, and one deeper in the volume (locations shown on Fig. 3C in the main text). $\gamma(h)$ was calculated for 70 linearly spaced separation distances up to h = 2 km from a subset of 30,000 points randomly selected from the extracted subregion. For each subregion, the resulting experimental variograms exhibit spatial structure, except the non-corrugated portion of the shallow megathrust, which exhibits a fractal-like behavior in the experimental variogram calculated down-dip direction. A weak periodicity is evident in the results for the shallow corrugated portion of the fault (perpendicular to the corrugations) where $\gamma(h)$ fluctuates about the sill in a periodic manner.

We treated the amplitude measurements as realizations of a spatial random function satisfying the intrinsic hypothesis [44], and fitted the calculated $\gamma(h)$ values for each dataset with a variogram model [47] to estimate the correlation distances (example shown in Extended Data Fig. 7). We selected a spherical model type with zero nugget effect, following the approach used in previous studies of fault structures [48,49]. Correlation distances estimated from the models (i.e., fitted α values) are listed in Extended Data Table 2.

Data Availability

The 3-D pre-stack depth-migrated seismic reflection data collected as part of Seismic Project MGL1106 Costa Rica Seismogenesis Project (CRISP) are available in the data repository at http://www-udc.ig.utexas.edu/sdc/ with identifier doi: 10.1594/IEDA/500204. The megathrust reflection geometry, depth beneath sea floor, and amplitude for the region shown in Figure 3 is available at: osf.io/3nxgb.

Code Availability

The code used to generate the apparent dip ('dip-steering') volume, dip-steered median filtered data can be accessed at https://github.com/OpendTect/OpendTect.

Methods References

29 Bangs, Nathan L.; McIntosh, Kirk D.; Silver, Eli; Kluesner, Jared; Ranero, Cesar. Processed 3D volume of multi-channel seismic data offshore western Costa Rica acquired during the R/V Marcus G. Langseth expedition MGL1106 (2011) as part of the Costa Rica Seismogenesis Project (CRISP). Academic Seismic Portal at UTIG, Marine Geoscience Data System. http://dx.doi.org/10.1594/IEDA/500204 (2018).

30 Knapp, R. W. VERTICAL RESOLUTION OF THICK BEDS, THIN BEDS, AND THIN-BED CYCLOTHEMS. *Geophysics* **55**, 1183-1190, doi:10.1190/1.1442934 (1990).

31 Ricker, N. The form and laws of propagation of seismic wavelets. *Geophysics* **18**, 10-40 (1953).

32 Rafaelsen, B. *et al.* Geomorphology of buried glacigenic horizons in the Barents Sea from three-dimensional seismic data. *Glacier-Influenced Sedimentation on High-Latitude Continental Margins* **203**, 259-276, doi:10.1144/gsl.sp.2002.203.01.14 (2002).

33 Thomson, D. J. SPECTRUM ESTIMATION AND HARMONIC-ANALYSIS. *Proceedings of the Ieee* **70**, 1055-1096, doi:10.1109/proc.1982.12433 (1982).

34 Brune, J. N. TECTONIC STRESS AND SPECTRA OF SEISMIC SHEAR WAVES FROM EARTHQUAKES. *Journal of Geophysical Research* **75**, 4997-&, doi:10.1029/JB075i026p04997 (1970).
35 Brune, J. N. SEISMIC SOURCES, FAULT PLANE STUDIES AND TECTONICS. *Transactions-American Geophysical Union* **52**, I178-+ (1971).
36 Boatwright, J. SPECTRAL THEORY FOR CIRCULAR SEISMIC SOURCES - SIMPLE ESTIMATES OF SOURCE DIMENSION, DYNAMIC STRESS DROP, AND RADIATED SEISMIC ENERGY. *Bulletin of the Seismological Society of America* **70**, 1-27 (1980).
37 Aki, K. & Richards, P. G. *Quantitative Seismology*. 2nd edn, (University Science Books, 2002).
38 Mori, J. & Frankel, A. SOURCE PARAMETERS FOR SMALL EVENTS ASSOCIATED WITH THE 1986 NORTH PALM-SPRINGS, CALIFORNIA, EARTHQUAKE DETERMINED USING EMPIRICAL GREEN-FUNCTIONS. *Bulletin of the Seismological Society of America* **80**, 278-295 (1990).
39 Abercrombie, R. E. Investigating uncertainties in empirical Green's function analysis of earthquake source parameters. *J. Geophys. Res.-Solid Earth* **120**, 4263-4277, doi:10.1002/2015jb011984 (2015).
40 Abercrombie, R. E., Bannister, S., Ristau, J. & Doser, D. Variability of earthquake stress drop in a subduction setting, the Hikurangi Margin, New Zealand. *Geophysical Journal International* **208**, 306-320, doi:10.1093/gji/ggw393 (2017).
41 Viegas, G., Abercrombie, R. E. & Kim, W. Y. The 2002 M5 Au Sable Forks, NY, earthquake sequence: Source scaling relationships and energy budget. *J. Geophys. Res.-Solid Earth* **115**, doi:10.1029/2009jb006799 (2010).
42 Eshelby, J. D. THE DETERMINATION OF THE ELASTIC FIELD OF AN ELLIPSOIDAL INCLUSION, AND RELATED PROBLEMS. *Proceedings of the Royal Society of London Series a-Mathematical and Physical Sciences* **241**, 376-396, doi:10.1098/rspa.1957.0133 (1957).
43 Madariaga, R. DYNAMICS OF AN EXPANDING CIRCULAR FAULT. *Bulletin of the Seismological Society of America* **66**, 639-666 (1976).
44 Kitanidis, P. K. *Introduction to geostatistics: applications in hydrogeology*. 249 (Cambridge University Press, 1997).
45 Experimental (Semi-) Variogram (MATLAB Central File Exchange, 2013).
46 Remy, N., Boucher, A. & Wu, J. *Applied geostatistics with SGeMS: a user's guide*. (Cambridge University Press, 2009).
47 variogramfit (MATLAB Central File Exchange, 2010).
48 Kirkpatrick, J. D., Shervais, K. A. H. & Ronayne, M. J. Spatial Variation in the Slip Zone Thickness of a Seismogenic Fault. *Geophys. Res. Lett.* **45**, 7542-7550, doi:10.1029/2018gl078767 (2018).
49 Lunn, R. J., Shipton, Z. K. & Bright, A. M. How can we improve estimates of bulk fault zone hydraulic properties? *Geological Society, London, Special Publications* **299**, 231-237, doi:doi:10.1144/SP299.14 (2008).
50 Kirkpatrick, J. D. & Brodsky, E. E. Slickenline orientations as a record of fault rock rheology. *Earth and Planetary Science Letters* **408**, 24-34, doi:10.1016/j.eps1.2014.09.040 (2014).

51 Ryan, W. B. F. *et al.* Global Multi-Resolution Topography synthesis. *Geochemistry Geophysics Geosystems* **10**, doi:doi: 10.1029/2008GC002332 (2009).

Extended Data

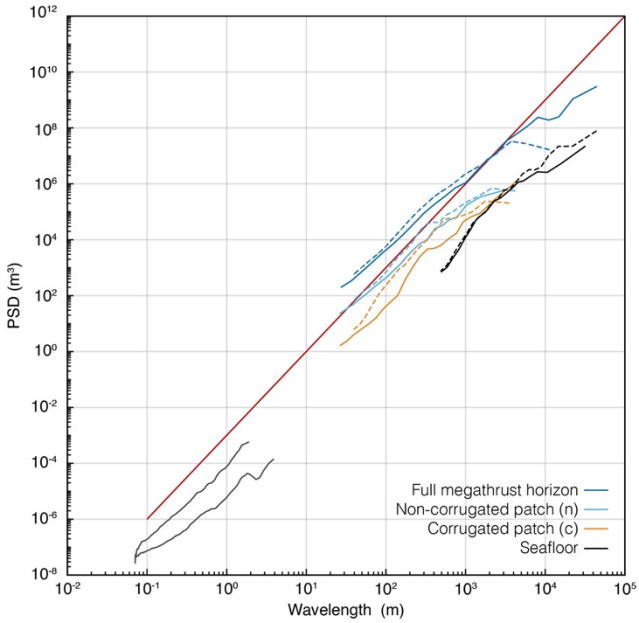

Extended Data Figure 1. **Megathrust power spectral density roughness compared to roughness calculated from ground-based LiDAR (Light Detection and Ranging) survey of an exposed ancient fault**. Data are the same as in Figure 3 in the main text except for the dark grey lines at short wavelength, which are calculated from the Corona Heights Fault [50]. Red line has a Hurst scaling exponent of 1 for reference.

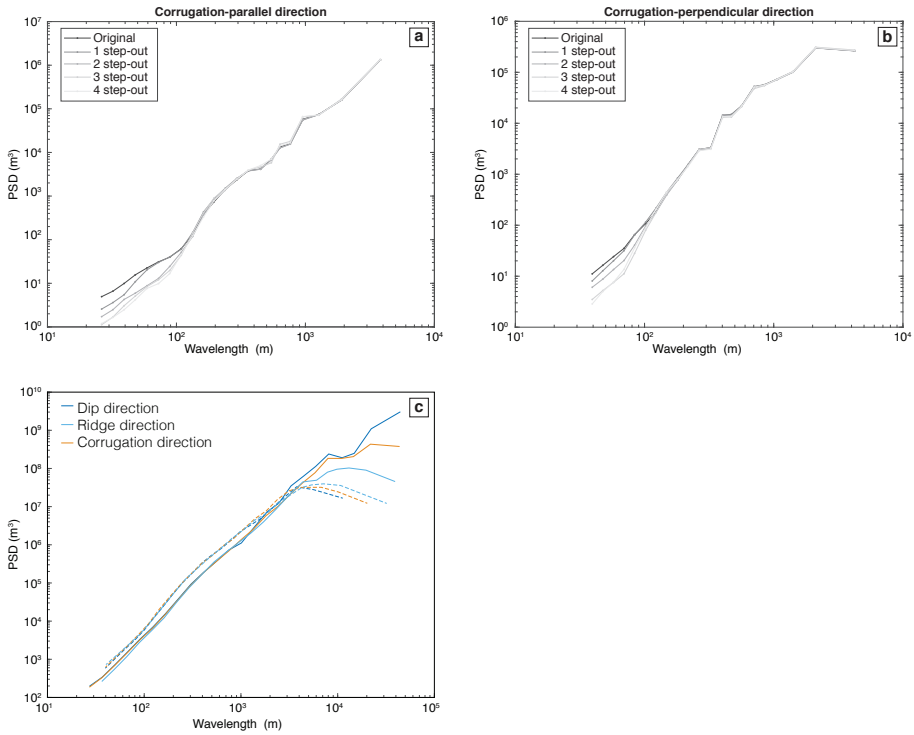

Extended Data Figure 2. **Analysis of the effect of the seismic volume attributes on roughness estimates**. A. Effect of dip-steered median filter step-outs on roughness measurements in corrugation-parallel direction. Comparison of calculated power spectral density from the shallow, well-corrugated portion of the megathrust horizon extracted from seismic volumes filtered with difference dip-steered median filter step-outs (inline x crossline). B. Same as A but for corrugation-perpendicular direction. C. Comparison of the megathrust power spectral density roughness calculated in different directions to test if the orientation of the megathrust dataset with respect to the coordinate system affected the length scale at which spectra calculated in perpendicular directions converge. Rotating the data around an axis normal to the mean plane through the dataset changes the number of profiles with different lengths, particularly the number of long profiles, and therefore the number of estimates of the PSD at long wavelengths. Roughness was calculated from profiles taken parallel and perpendicular to three reference directions: down dip and across strike; parallel and perpendicular to the corrugations present at shallow depths; perpendicular and parallel to the ridge axes in the middle portion of the megathrust. Differences in PSD at length scales > 5 km result from the smaller number of the longest profiles following rotation of the data around the Z-axis to the different

reference directions. These results show the length scale of convergence is approximately the same in each pair of spectra.

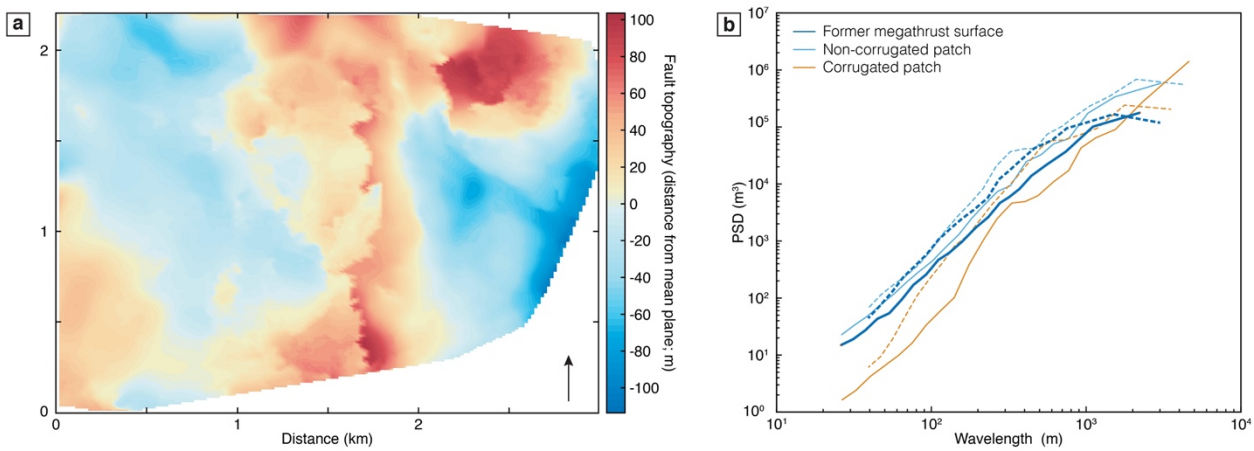

Extended Data Figure 3. **Example of an abandoned megathrust horizon extracted from the footwall at around 19 km landward of the trench**. A. Map of the surface topography. Colors correspond to distance from the mean plane fitted through the region shown. Dip direction indicated by arrow. B. Power spectral density roughness of the abandoned megathrust horizon (bold lines) shown in A. This patch shares similar characteristics to the in-situ megathrust, being anisotropic and smoother in the direction of visible corrugations. Spectra for the corrugated and non-corrugated patches from Figure 2 in the main text are shown for reference. The roughness of the abandoned horizon is intermediate between the corrugated and weakly corrugated portions of the shallow megathrust.

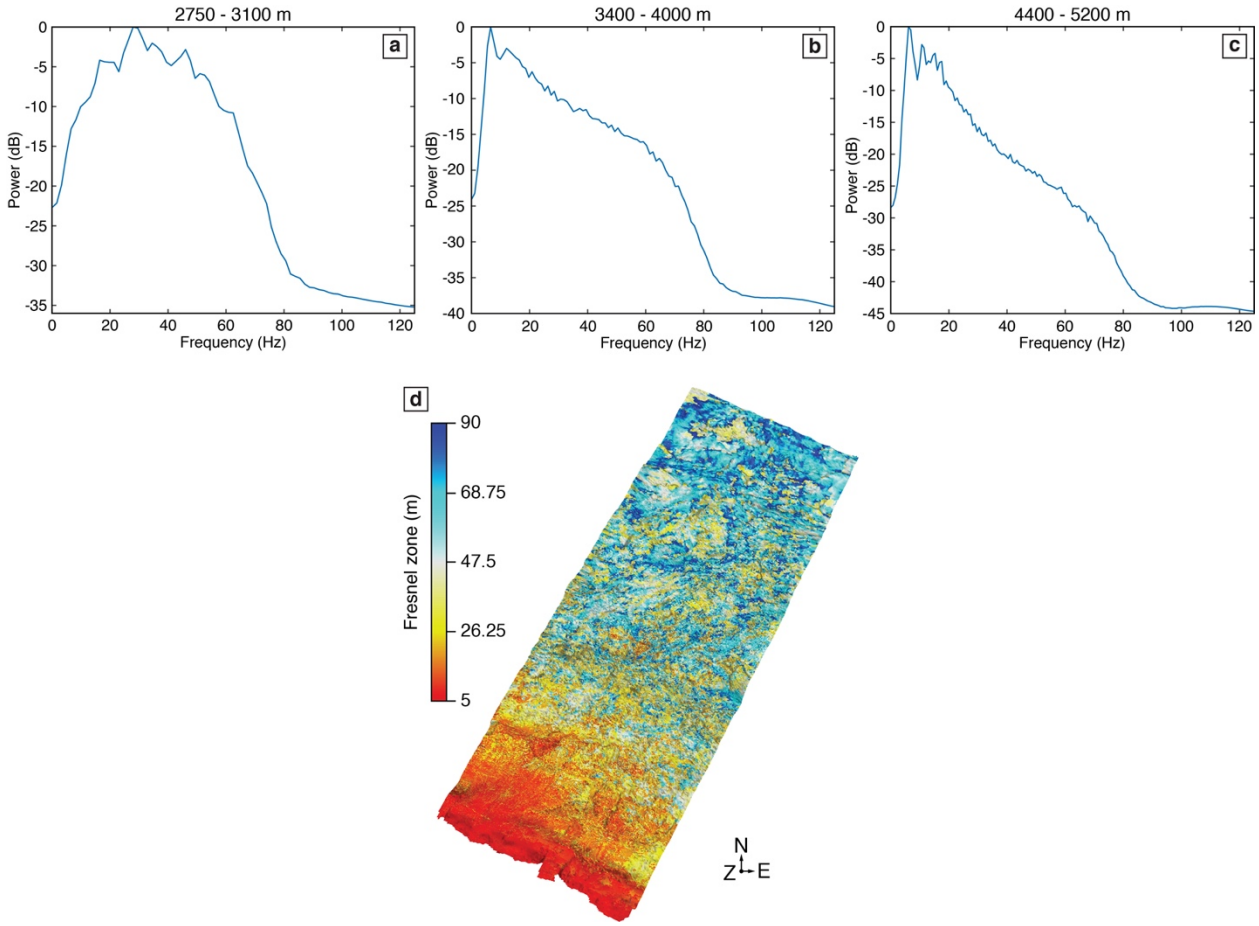

Extended Data Figure 4. Analysis of 3-D seismic volume spatial resolution. A, B, C: Amplitude histograms of the megathrust reflection from different depth intervals. Seismic bandwidth decreases (attenuation of high frequencies) with increasing depth. D. Post-migrated Fresnel zone variation with depth. Fresnel zone size increases with depth.

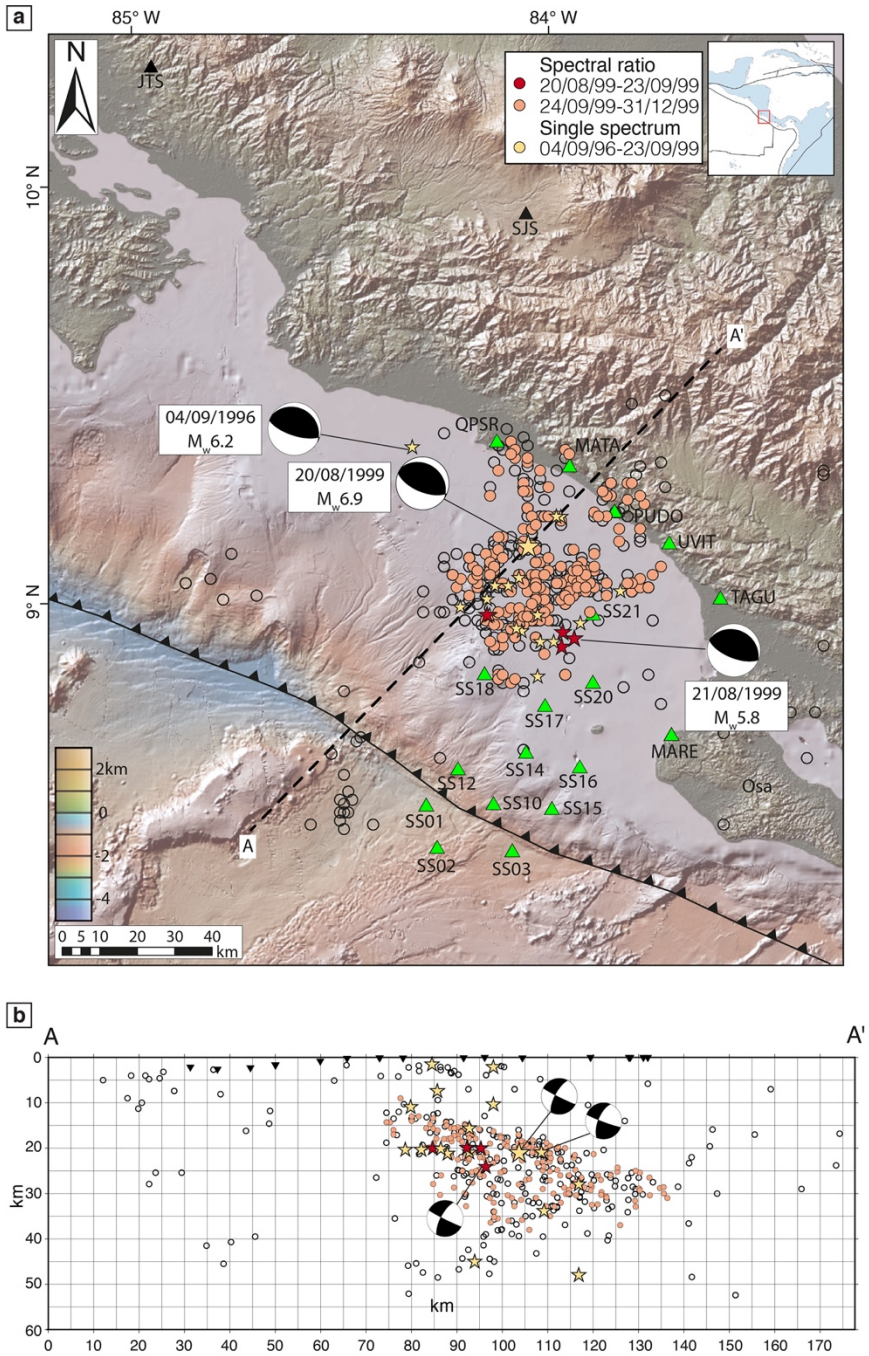

Extended Data Figure 5. **Map and cross section of earthquakes for source parameter estimates**. A. Overview map with bathymetry [51] of the study region. Circles represent aftershocks occurring between September 1999 and November 1999 [25]. Pink circles indicate earthquakes considered here occurring on the plate interface, for which corner frequencies are calculated using the spectral ratio method. Red stars are the earthquakes that occurred between August 20, 1999 and September 24, 1999, for which corner frequencies are calculated using the

spectral ratio method. Yellow stars are the mainshock (big star), and earthquakes (small stars) that occurred between September 9, 1996 and September 23, 1999, for which corner frequencies are calculated using the single spectrum method. Green triangles are the CRSEIZE seismometer locations, and black triangles are RSN (SJS) and IRIS/IDA (JTS) station locations. Dashed black line indicates the location of the cross section below. B. Cross section showing earthquake hypocentral depths. Symbols as in A. Inverted triangles indicate locations of seismic stations.

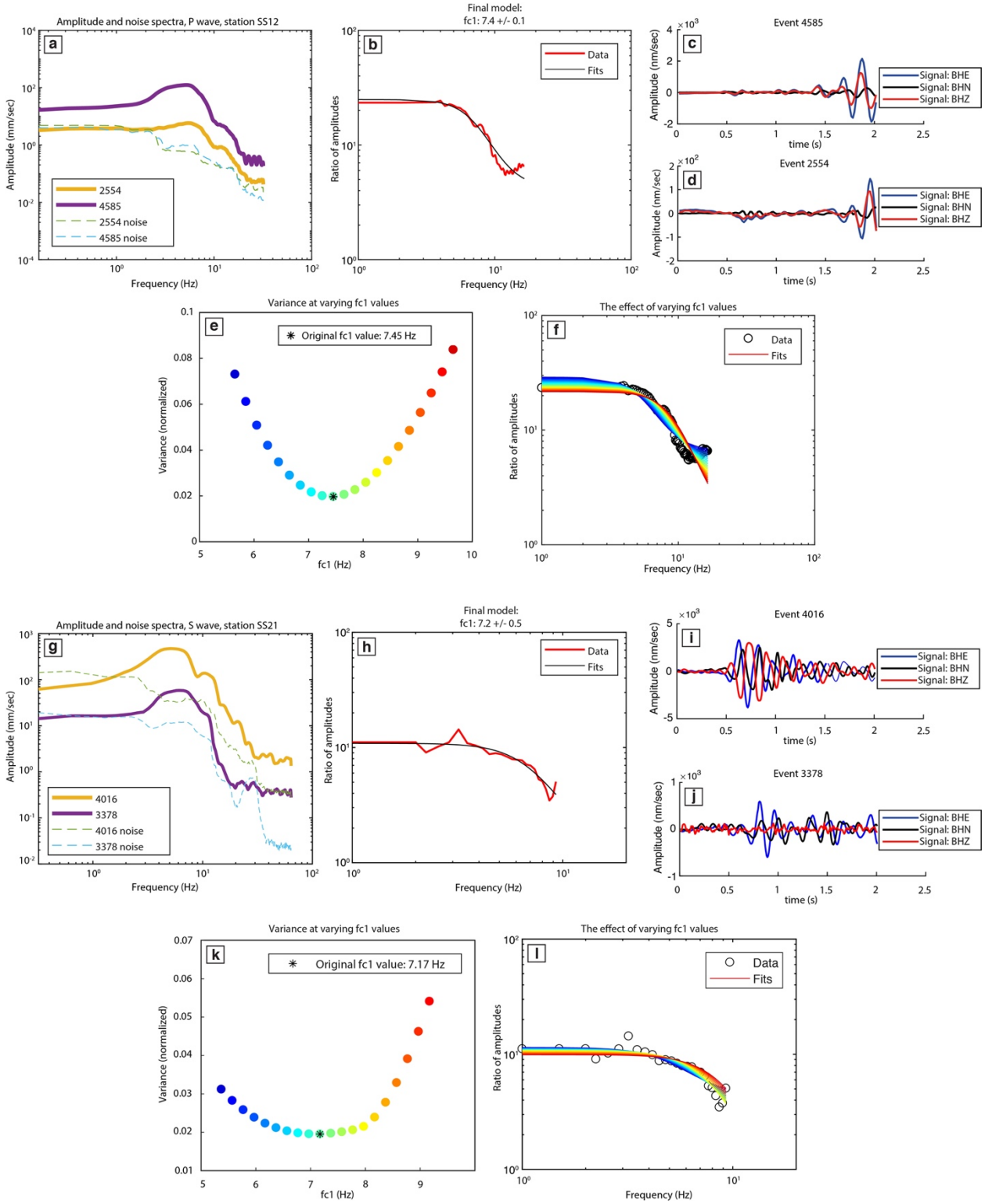

Extended Data Figure 6. **Examples of waveform analyses**. A-F: Spectral ratio fits for the event pair 4585 (Mw=2.6) and 2554 (Mw=1.9) having CC=0.8. A. Single spectra amplitude and noise spectra of each event. B. Spectral ratio and the model fit with the final corner frequency

estimates. C. and D. Waveforms in the time domain. E. The variance (chi-square misfit) for incremented values of fc1, each value represented by a different color. F. Corresponding fits to the data at different fc1 increments. G-L. Spectral ratio fits for the event pair 4016 (Mw=1.8) and 3378 (Mw=1.3) having CC=0.7. G. Single spectra amplitude and noise spectra of each event. H. Spectral ratio and the model fit with the final corner frequency estimates. I. and J. Waveforms in the time domain. K. The variance (chi-square misfit) for incremented values of fc1, each value represented by a different color. L. Corresponding fits to the data at different fc1 increments.

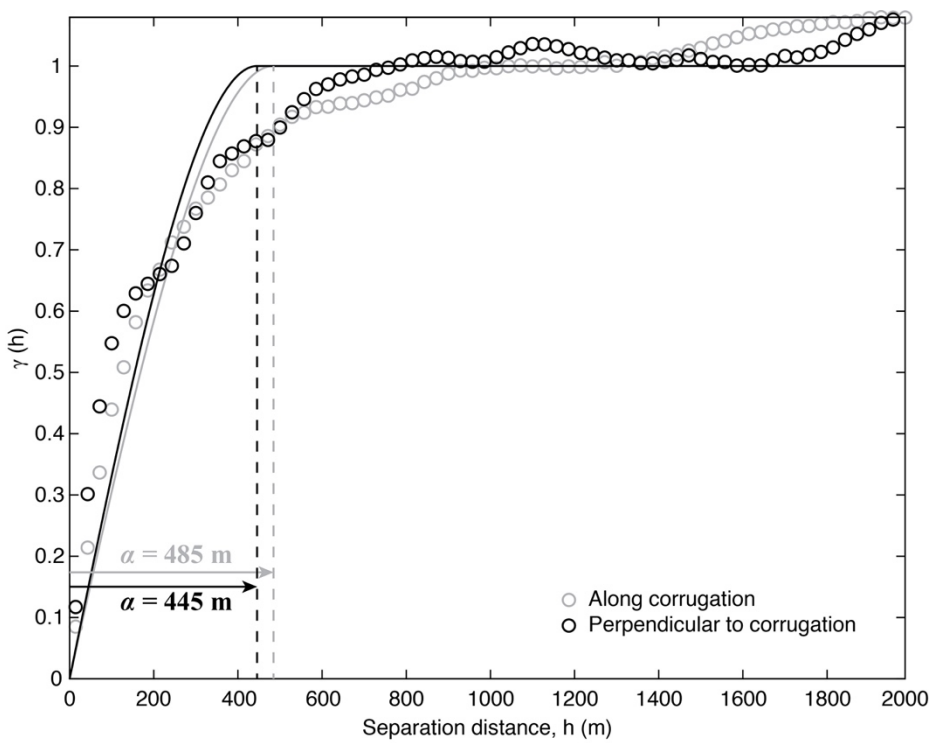

Extended Data Figure 7. **Geostatistical analysis of the amplitude field from the corrugated subregion of the shallow megathrust**. $\gamma(h)$ shown here is the same as in Fig. 3E of the main text. The results clearly show that $\gamma(h)$ attains a constant value for large h (normalized to 1 here). The curves through the results represent model fits to experimental variograms, which have correlation distances, α, of 485 and 445 m in the two perpendicular reference directions.

	Time	Method	M[a]	Relocated	CC[b]	Time-window (sec)[c]	Magnitude difference[d]	Stations
1	24.09.1999-31.12.1999	Spectral ratio	1.6-3.3	Yes	0.7	2	0.5	CRSEIZE
2	20.08.1999-23.09.1999	Spectral ratio	4.3-5.8	No	0.7	7	0.5	JTS, SJS
3	04.09.1996-23.09.1999	Single spectrum	3.6-6.9	No	/	7, 15	/	JTS, SJS

[a]Magnitude range. [b]Correlation Coefficient. [c]Time-window around P and S-waves used for spectral estimations. [d]Minimum magnitude difference between the larger event and its EGF for spectral ratio calculations.

Extended Data Table 1. Summary of data sources and methods used to estimate the source parameters plotted in the figures in the main text.

[a]Magnitude range. [b]Correlation Coefficient. [c]Time-window around P and S-waves used for spectral estimations. [d]Minimum magnitude difference between the larger event and its EGF for spectral ratio calculations.

We divided the studied earthquakes in three groups. Group 1 (pink in the figures) includes aftershocks from the M 6.9 mainshock (20/08/1999), for which we calculated source parameters using the spectral ratio method. These events were recorded by the OBS broadband stations (CRSEIZE) and relocated by [25]. The second group (red stars in the figures) includes four aftershocks occurred before the deployment of the CRSEIZE network. For these events we calculated source parameters using the spectral ratio method, but in this case, we used only land stations from the Costa Rican (SJS) and IRIS (JTS) networks. Finally, group 3 (yellow stars in the figures) includes earthquakes possibly occurred on the subduction interface between 04/09/1996, when a M 6.2 event occurred, and 23/09/1999. Among these events the M 6.9 mainshock (20/08/1999) is also included. The difference between this group and groups 1 and 2 is that for the earthquakes included in group 3 we could not find any pairs of events with a correlation coefficient larger than 0.7, which is the minimum requirement we established to consider two events co-located. Therefore, we could not calculate source parameters using the spectral ratio method. We used instead single spectra.

Area	Direction	Correlation distance, α (m)
Corrugated	Dip	485
	Strike	445
Non-corrugated	Dip	Unbounded
	Strike	491
Mid-depth	Dip	312
	Strike	310
Deep-depth	Dip	417
	Strike	549

Extended Data Table 2. **Correlation distances obtained from model fits to the experimental variograms shown in Figure 3 in the main text.**